LETTER

Self–assembly of graphene ribbons by spontaneous self–tearing and peeling from a substrate

James Annett[1,2,3] & Graham L. W. Cross[1,2,3]

Graphene and related two-dimensional materials have shown unusual and exceptional mechanical properties[1–3], with similarities to origami-like paper folding[4,5] and kirigami-like cutting[6,7] demonstrated. For paper analogues, a critical difference between macroscopic sheets and a two-dimensional solid is the molecular scale of the thin dimension of the latter, allowing the thermal activation of considerable out-of-plane motion. So far thermal activity has been shown to produce local wrinkles in a free graphene sheet that help in theoretically understanding its stability[8], for example, and give rise to unexpected long-range bending stiffness[6]. Here we show that thermal activation can have a more marked effect on the behaviour of two-dimensional solids, leading to spontaneous and self-driven sliding, tearing and peeling from a substrate on scales approaching the macroscopic. We demonstrate that scalable nanoimprint-style contact techniques can nucleate and direct the parallel self-assembly of graphene ribbons of controlled shape in ambient conditions. We interpret our observations through a simple fracture-mechanics model that shows how thermodynamic forces drive the formation of the graphene–graphene interface in lieu of substrate contact with sufficient strength to peel and tear multilayer graphene sheets. Our results show how weak physical surface forces can be harnessed and focused by simple folded configurations of graphene to tear the strongest covalent bond. This effect may hold promise for the patterning and mechanical actuating of devices based on two-dimensional materials.

In this Letter we report how the thermal activation of the thin dimension of a two-dimensional solid allows it to undergo self-tearing, sliding and folding, which result in substantial mass transport. In Fig. 1 we show spontaneous, large-scale motion of graphene. A single-layer sheet was mechanically exfoliated onto a 300 nm thermal oxide layer on a silicon wafer (optical micrograph Fig. 1a) and then heated to 150 °C on an open hot plate for 13 d. The subsequent optical micrograph of the flake in Fig. 1b shows a large, folded-over flap formed by a 5 μm horizontal tear in the top of the flake combined with a straight, vertical fold that is over 20 μm in length. A series of steps that might have led to the formation of this flap is proposed in the schematics of Fig. 1c–e: the process was initiated by the formation of a small, stable folded-over tab (Fig. 1c). We assume that this tab is too small to see in the optical micrograph of Fig. 1a, and was probably created as an unintended by-product of the original mechanical nucleation process. This embryonic structure then grew by sliding and peeling, and eventually also tearing, as it evolved from Fig. 1c–e.

To justify and explain this proposed formation sequence, in the lower half of Fig. 1 we demonstrate a deterministic mechanical method that allows the controllable nucleation of an embryonic fold such as that in the schematic in Fig. 1c, which then results in a spontaneous growth process. In Fig. 1f–l, a time series of atomic force microscopy (AFM) images reveals the formation of three elongated ribbons in bilayer graphene that decorate a triangular indentation crater of about 1 μm in size. The crater was formed by performing ambient, room-temperature

nanoindentation using a pyramidal diamond Berkovich tip with a load sufficient to pierce the sheet and permanently indent the substrate below. Critical to the success of the method was the presence of a small amplitude (∼1 nm) lateral shearing oscillation imposed at high frequency throughout the indentation process. This fretting action was found to form small tabs of folded-over, adhered graphene—an example of which is shown in the inset of Fig. 1l. The fretting was necessary to realize growing ribbon structures (>70% yield with fretting versus 0% without, with over 100 ribbons produced in one-, two-, three- and four-layer graphene, see Fig. 1n for an example of high-yield production.) For the three ribbons nucleated in Fig. 1l, each had a starting width of about 0.6 μm and tapered inwards with a ∼15° angle. The upper ribbon (1) grew to length of ∼1.5 μm, whereas the lower left ribbon (2) encountered and grew over a subsheet defect before also stopping at ∼1.5 μm in length. The ribbon on the right (3) halted at ∼0.7 μm in length when it encountered the flake edge. A time-lapse movie of this 14 day process can be found in Supplementary Information.

We have produced ribbons with starting widths of ∼300 nm to >2,000 nm by varying the indentation depth; some of these ribbons were observed grow to >5 μm in length. Heating the samples above room temperature (either globally on a hot plate or locally using a focused laser spot) increased the nucleation probability and generally accelerated and expanded growth, however, the majority of our ribbons were nucleated and grew at room temperature. Once underway, most of the length of a ribbon formed on a timescale shorter than AFM imaging (which is on the order of minutes), but then continued slowly, decelerating smoothly over any period of continued image capture that we used. Ribbon growth could be stochastic, sometimes impeded by obvious external defects or contaminants (see Extended Data Fig. 1) that were pushed aside or otherwise overcome to allow rapid growth to resume. Although many ribbons grew in a symmetric fashion, deviations were observed. Collisions with defects, contamination, flake edges and other ribbons—or varying conditions such as temperature during growth—produced asymmetric, transient fold bulging with variable, asymmetric or even negative tapering. This led to asymmetry in ribbon shape and rotation of the growth direction.

Analysis of the strips peeled from adhered macroscopic films has shown how tearing forces and strip tapering angles depend on adhesion, fracture toughness and elastic strain energy within the fold[9,10]. In our case, peeling of the graphene strips is clearly not the result of an external force[11], but instead, we propose, the result of a thermodynamic mechanism of exchanging graphene–substrate area with graphene–graphene area. We refer to this as the interfacial force, arising from the difference in the energy release rates of peeling and healing along the entire width of the ribbon at the attaching fold. Our system thus consists of a closing adhesive crack that drives the tearing of two covalent cracks, sliding of the ribbon head and peeling from the substrate.

For sufficiently wide ribbons, we find that the net exchange of interfacial energy is sufficient to produce motion forwards against the forces of sliding and tearing resistance. The stability of this folded configuration

[1]Centre for Research on Adaptive Nanostructures and Nanodevices, Trinity College, Dublin 2, Ireland. [2]Advanced Materials and BioEngineering Research, Trinity College, Dublin 2, Ireland. [3]School of Physics, Trinity College, Dublin 2, Ireland.
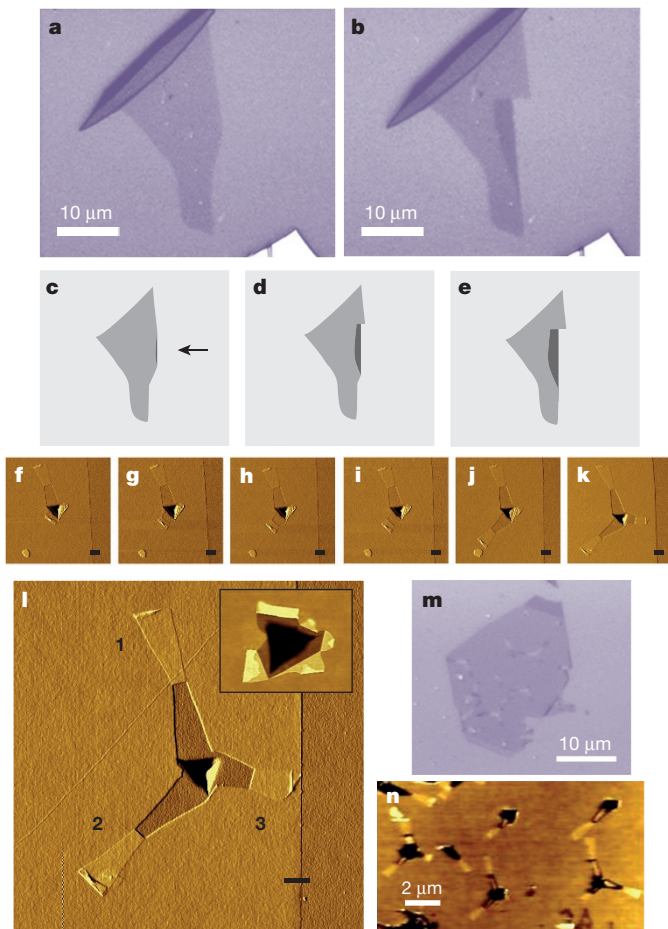
Figure 1 | Self assembly of graphene flaps and ribbons. a–e, A self-folded graphene flap formed by spontaneous folding, sliding, peeling and tearing of a single-layer sheet adhered to a silicon oxide substrate. **a, b**, Optical micrographs taken before (**a**) and after (**b**) the spontaneous formation of a 20-μm-long folded flap by tearing back from the right-hand edge of the flake. The system was heated to 150 °C in ambient conditions for 13 d between **a** and **b**. The final area of the measured flap is approximately 50 μm^2. **c–e**, A proposed series of steps leading to the formation of the tab is shown, with an initial nucleating fold indicated by the black arrow in **c**, and progressive growth by sliding and tearing in **d**, to the final position in **e**. **f–n**, Directed graphene ribbon self-assembly by nanoindentation. **f–l**, AFM image sequence of room-temperature, ambient condition growth of three ribbons nucleated from single fretted nanoindentation contact (similar to the inset in **l**) in bilayer graphene over a period of 14 days. Panels **f**, **g**, **h**, **i** and **j** show progressive stages in the growth of ribbon 2. Ribbon 2 grows over a sub-sheet defect in **k** and **l**, whereas ribbon 3 starts growth between **j** and **k** and ceases growth prematurely at the flake edge in **l**, avoiding growth onto the silicon oxide substrate. A time lapse movie of this growth is provided in Supplementary Information. Scale bars, 500 nm. **m**, Optical micrograph of high-yield, multiple ribbon growth events nucleated by fretted contact in a bilayer graphene flake. **n**, AFM image of the central portion of **m** at higher magnification.

is enabled by a length of graphene–graphene surface interaction that overcomes its own folding strain energy U_{fold}, similar to the structure of collapsed nanotubes[12,13] or a self-adhered graphene 'tennis racket'[4,14], but altered by adherence to the rigid flat substrate[15–17]. We expect the strain energy contained within the fold to influence the fracture path, reducing the width of the fold[9].

In the following we present an analysis of the forces acting during the final stages of ribbon growth to give physical insight into the overall formation process. An AFM image of a ribbon formed from a trilayer graphene flake and with no (or imperceptibly slow) growth is shown in Fig. 2c, along with height profiles (Fig. 2a, b) extracted from the image,

indicating the presence of a folded ridge with a protruding height of about 0.4 nm and a width of less than ~20 nm (which is the lateral resolution of our image). From a nucleated width w_0 of ~0.8 μm, the ribbon is formed by tearing mirror-symmetric, straight fracture paths, each of which tapers inwards with taper half-angle θ of ~6° with respect to the growth axis, reaching a final length l of ~2.1 μm and a final folded ridge width w of ~0.4 μm. The ribbon head position h is also indicated. In the absence of contaminants, this form of ribbon growth is typical, exhibiting symmetric, inward tapering at a small, constant tapering angle with a highly symmetric, tightly folded and straight ridge terminated by two sharply defined tearing points. Invoking a Griffith-style elastic fracture analysis[18], we assume that the host graphene sheet that contains the ribbon shown with area A_{ribbon} has total area A_{sheet} and write the internal energy of the system as

$$U = U_{fold} + 2\lambda c + \gamma_1(A_{sheet} - A_{ribbon}) + \gamma_2 A_{ribbon} \qquad (1)$$

where λ is the rupture energy per unit of length required to tear the sheet (which ignores the orientation effects of crystallography), γ_1 is the adhesion energy of the sheet to the substrate, γ_2 is the adhesion energy of the sheet to itself and c is the path length of the two tears (assumed to be identical) that define the ribbon shape.

In general, for a two-dimensional material with a given number of layers and bending stiffness D, the strain energy U_{fold} will depend on the un-adhered excess ribbon length $\zeta = 2l - h$ contained in the fold as well as w (ref. 9), expressed explicitly as $U_{fold}(\zeta, w) = wD \int_0^\zeta \kappa^2(s)\,ds$ where $\kappa(s)$ is the curvature of the sheet at path position s in the folded region. However, similar to self-adhered folding in free graphene strips[14], we expect in our system that beyond a minimum ribbon length, the cross-sectional fold shape (Fig. 2c, lower inset) becomes constant (that is, ζ becomes constant) and $U_{fold} = U_{fold}(w)$ only. Assuming for the moment that no friction is associated with the sliding of the adhered ribbon over its host sheet, we compute the fracture energy release rate[18] of our system for a simultaneous increment δc of both tears under our interfacial force to be

$$\frac{\delta U}{\delta c} = \frac{\delta U_{fold}}{\delta w}\frac{\delta w}{\delta c} - (\gamma_2 - \gamma_1)w\frac{\delta l}{\delta c} + 2\lambda \qquad (2)$$

Under our quasi-static, end-of-growth conditions, we have a balance of forces acting at each crack tip and the energy release rate must be zero[18]. Noting that $(\delta l/\delta c) = \cos\theta$, $(\delta w/\delta c) = -2\sin\theta$ and letting $S = \int_0^\zeta \kappa^2(s)\,ds$ remain constant, we divide the advancing and resisting effects equally between the two tears and from equation (2) can write the forces acting at each crack tip as

$$F_{advance} = \frac{\gamma_2 w \cos\theta}{2} + DS\sin\theta = \frac{\gamma_1 w \cos\theta}{2} + \lambda = F_{resist} \qquad (3)$$

as shown in the upper schematic of Fig. 2c.

Projecting the forces derived in equation (3) along the direction of ribbon propagation, we find at each crack tip

$$\frac{(\gamma_2 - \gamma_1)w}{2} = \lambda\cos\theta \qquad (4)$$

Experimentally, the dominant direction for fracture growth is found to be at right angles to the fold (that is, we have small θ), here seen to be driven by the net interface tension (difference between healing and peeling force) $(\gamma_2 - \gamma_1)w$ overcoming most of the tearing resistance. Along the fold direction (that is, orthogonal to the ribbon propagation direction) we find that $DS = \lambda\sin\theta$ where an energetically favourable tendency to reduce the fold energy[9] manifests as a small, inward taper force working against a small tearing resistance component. These projections are also represented in the upper schematic of Fig. 2c. The maximum energy release rate criterion of fracture mechanics dictates that the tear will take the path of minimum force[18], found by minimizing
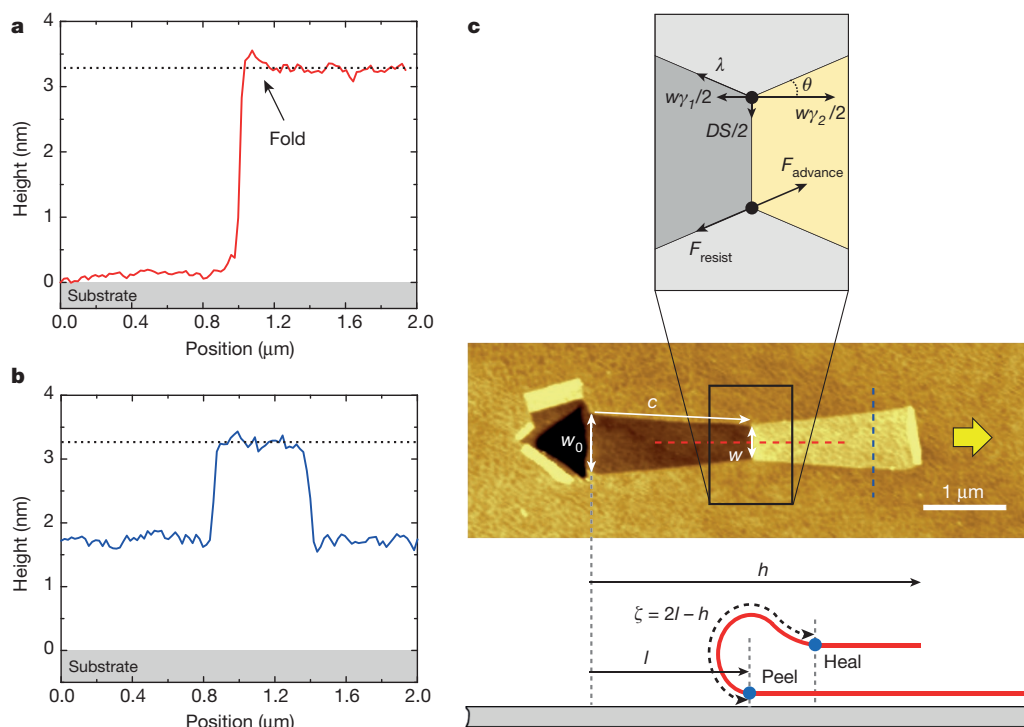
Figure 2 | Fracture mechanics analysis of quasi-static ribbon growth. a, b, Cross-sectional profiles extracted from **c** (along the dashed red and blue lines) of a typical self-assembled ribbon undergoing slow, quasi-static growth with symmetric, constant tapering in trilayer graphene. The dashed black lines indicate the top of the ribbon. **c**, AFM image of the ribbon with the geometric parameters of ribbon length l, head position h, nucleation fold width w_0 and final fold width w labelled. The upper schematic shows the plan view of two equivalent representations of the forces acting at each tearing crack tip (black dots) as well as the definition

of the taper half-angle θ. Ribbon growth occurs due to an interfacial healing crack with force magnitude $w\gamma_2/2$ focused at each tear tip, which overcomes the peeling and tearing resistances of $w\gamma_1/2$ and λ respectively. Inward taper occurs due to a tendency to reduce strain energy in the fold, manifesting as force $DS/2$ at each tip. The lower schematic is a side view of the ribbon showing a (highly zoomed) view of the fold cross-section with excess length $\zeta = 2l - h$ (dashed black curve between surface peel and heal points, indicated by blue dots). Ribbon growth direction is to the right, as indicated by the yellow arrow.

equation (3) with respect to θ. Performing this operation, we find the taper half-angle to be related to the ratio of the driving forces as

$$\tan\theta = \frac{2DS}{(\gamma_2 - \gamma_1)w} \quad (5)$$

The significance of small, constant taper angles observed for a majority of the ribbons is highlighted by equation (5). First, the presence of substantial frictional sliding should manifest as an extra force resisting growth in equation (4) and add to the denominator of equation (5). Classically, we expect friction to increase directly with ribbon area[19], thus the constant taper angle we observe for ribbons without externally impeded growth (that is, not affected by contamination) implies that friction is of negligible magnitude compared to the interfacial force. It seems that fold-constrained (that is, fixed-direction) sliding of graphene on supported graphene maintains low friction in ambient conditions as ribbons grow well above the micrometre scale. Sliding graphitic basal interfaces with incommensurate orientation have been shown to exhibit superlubricity on nanometre[20] to micrometre[21] scales, even in ambient conditions[22]. We have confirmed the incommensurate stacking of our ribbons using scanning Raman spectroscopy (see Extended Data Figs 2 and 3). This is consistent with observations in other systems of weak scaling of friction with area due to mismatched lattice structure at an atomically flat interface[19].

In the absence of friction, the steady attenuation of the driving interfacial force due to tapering as indicated by equation (4) suggests why ribbon growth stops at a finite width. In this case, ribbons nucleated with different starting widths should taper equivalently and terminate with the same final width under similar conditions. Figure 3a shows three bilayer graphene ribbons with parallel growth direction, nucleated with different starting widths in close proximity by nanoindentation.

This configuration gives a high probability that the ribbons will share the same surface adhesion conditions and crystallography of a single grain in the graphene. In Fig. 3b we overlay the traces of the ribbons to show that they share a common taper angle $2\theta \approx 12°$ and stopping width $w \approx 290\,\text{nm}$ despite the fact that each has a very different size and presumably different friction. To further investigate this, we have measured the shape of a population of 15 contamination-free ribbons that exhibit a constant taper angle in one-, two- and three-layer graphene. The final widths of our controlled population are plotted in Fig. 3c, which shows increasing final widths with an increasing numbers of layers. Assuming that the tearing resistance increases with the number of layers, this supports the assertion that ribbon growth is terminated by the decreasing interfacial force at a threshold width where it is insufficient to tear the graphene lattice. In principle, the stopping width and taper angle can be predicted from the sheet properties in equations (4) and (5), however the quantitative scaling behaviour of the graphene bending modulus[11,16] and adhesion[23–26] with layer number remains unclear, and compounded by our lack of knowledge of the local crystallography (which is expected to influence λ), we only report our measurements here.

Overall, our analysis suggests a picture of a well-adhered but easily sliding ribbon head, with the newly torn ribbon length drawn through a fold with an invariant cross-section that is held in constant strain per unit width by the balance of adhesion forces. Although we expect the angle of the inward tapering of the ribbon to slowly increase due to the taper-induced decrease of the interfacial force in equation (5), this is generally not apparent before ribbon growth ceases. Figure 3a also suggests that our ribbon self-assembly may be exploited to perform positive- or negative-tone lithography. Large-area scale-up of multiple nucleation sites should be readily achievable with multiple-tip nanoimprint-style stamps. The formation time of unimpeded
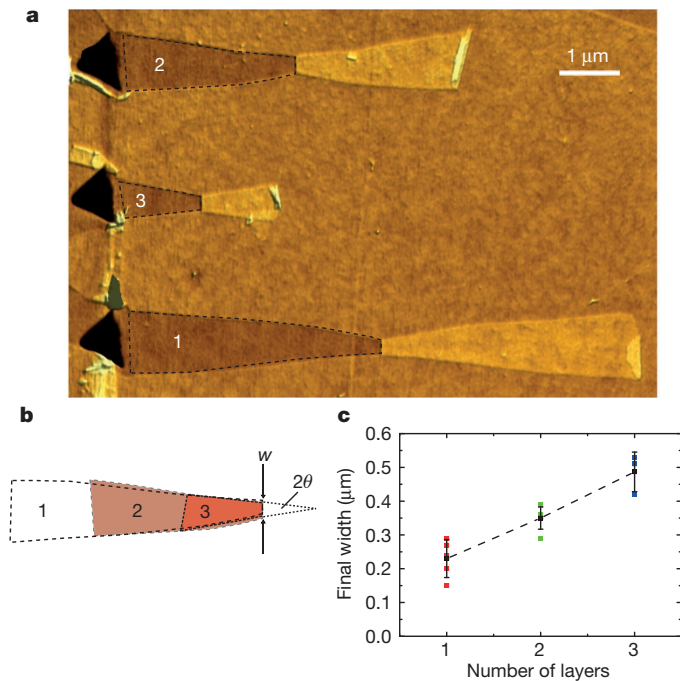
Figure 3 | Geometry of ribbon growth. a, Simultaneous growth of three ribbons (labelled 1–3) in bilayer graphene with different starting widths. **b**, Numbered trace overlays demonstrating that all three ribbons have a similar tapering angle $2\theta \approx 12°$ and identical final stopping width $w \approx 290$ nm . **c**, Plot of w versus the number of layers for a population of 15 ribbons including single-, bi- and trilayer graphene (shown in red, green and blue, respectively). The black squares indicate the mean final width for each layer count and the error bars show one standard deviation (the black dashed line is shown to guide the eye to the trend). The increase in the final width of the ribbons with layer number supports a picture of ribbon growth being arrested by the tearing resistance.

self-assembly is faster than AFM scanning can determine, and may indeed take place in a fraction of a second even at room temperature—similar to microscale graphitic pillar pull-in[22].

In the slow, terminal regime of ribbon growth we expect sheet tearing to be governed by lattice trapping, where a force insufficient to break the carbon bonds in the sheet is augmented by thermal activation[18]. In Fig. 4 an AFM image sequence of room-temperature bilayer ribbon growth is shown with an approximately constant taper angle, captured over a period of 3.5 h. The semi-logarithmic plot in Fig. 4 presents over two decades of smooth, decelerating ribbon growth velocity data fitted to the form

$$v = \nu_0 a_0 \left[\exp\left(-\frac{\lambda a_0}{k_B T} \right) \sinh\left(\frac{\alpha(\Delta\gamma - \beta)w}{k_B T} \right) \right] \quad (6)$$

where k_B is Boltzmann's constant, T is temperature, the natural lattice frequency $\nu_0 = k_B T/h \approx 6 \times 10^{12}$ s^{-1}, h is Planck's constant, a_0 is the spacing between the bonds along the crack path, α is the activation length, $\Delta\gamma = \gamma_2 - \gamma_1$ is the net interfacial energy difference and β embodies any active resistance terms beyond the substrate peeling and tearing (such as the friction of the ribbon head sliding or the internal fold inter-layer sliding), which we have assumed to also scale proportionally with ribbon width w. Equation (6) (derived in Methods with numerical analysis shown in Extended Data Fig. 4) relates the single-bond breaking, rate-activated velocity to ribbon width, where the latter quantity is assumed to be proportional to the crack-driving interfacial energy release rate. From the fit we extract a bond-rupture energy density of $\lambda \approx 30$ eV nm^{-1}, which is broadly compatible with simulations of the graphene tearing resistance[11,27]. If we further assume negligible dissipative processes (that is, $\beta = 0$), we find that the minimum difference in interface energies required to drive forward ribbon assembly in our
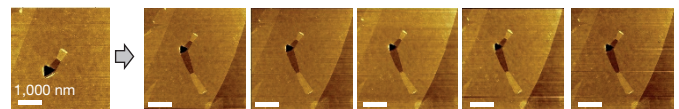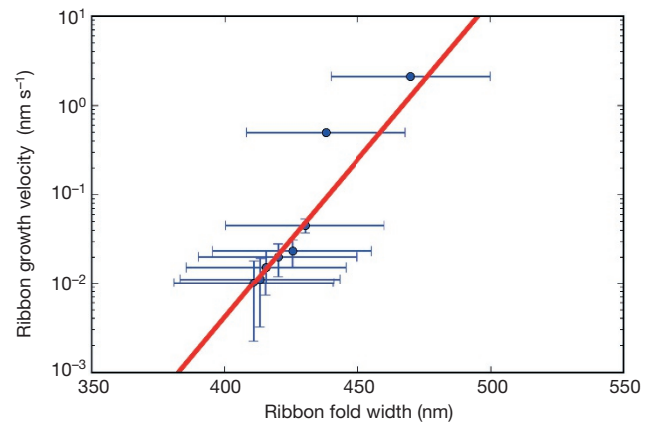
Figure 4 | Kinetics of self-assembling graphene ribbons. Semi-logarithmic plot of the velocity of ribbon growth in bilayer graphene versus the width of the ribbon fold w near the end of growth (the slow, quasi-static limit), showing evidence for stress-activated sheet rupture and frictionless sliding driven by interfacial adhesion forces that are proportional to the ribbon width. Data was extracted from the ribbon growing in the lower right of the sequence of AFM images shown below the plot. Unlabelled scale bars, 2 μm. The error bars in the plot indicate the standard deviation of the width and length measurements from the images.

sample is ~0.02 eV nm^{-2}, which we note is only a small fraction of the adhesion energies that have been determined for graphene–solid inter-faces, which are on the order of 1 eV nm^{-2} (refs 23–26). Multiplying this surface energy difference by the terminal width of ~350 nm we compute an interfacial driving force of approximately 1 nN. This value is slightly lower than the expected carbon bond strength of a few nano-newtons, consistent with fracture propagation at a sub-critical force for bond breaking. From this we infer that a slight increase in the adhesive affinity from one surface to another can drive self-assembly, provided that there is free sliding.

Over 20 years ago, it was envisioned that graphene could be folded and cut into useful forms as a kind of nanoscale origami[5]. Our results suggest a much richer potential for two-dimensional materials: they can behave as a self-animated sheet that folds, tears and slides over itself in ambient conditions. Spontaneous ribbon growth offers a way to investigate the combined effects of adhesion, folding, sliding and tearing of two-dimensional sheets in a self-consistent way. The weakness of sliding friction indicates that the growth of sufficiently wide ribbons could in principle reach very large scales suitable for wafer-scale transfer processes, for example. There is the potential to control and scale the behaviour as a lithography to pattern and assemble two-dimensional materials, including incommensurate hetereo-stacks of dissimilar two-dimensional materials that may organize in novel ways depending on the strength of their interactions[28]. Surface functionalization may allow the manipulation of self-assembly by heat, light or other controllable external fields, enabling nanoelectro-mechanical systems of mechanically coupled sensors and actuators made up of two-dimensional materials. Fundamentally, the behaviour we have observed reveals a tendency for isolated two-dimensional matter to coalesce towards a lower-energy three-dimensional form if kinetic barriers are overcome. The constrained sliding and folding pathways required to approach equilibrium may allow new arrange-ments and usages of two-dimensional materials to be realized through self-assembly.

Online Content Methods, along with any additional Extended Data display items and Source Data, are available in the online version of the paper; references unique to these sections appear only in the online paper.

1. Rasool, H. I., Ophus, C., Klug, W. S., Zettl, A. & Gimzewski, J. K. Measurement of the intrinsic strength of crystalline and polycrystalline graphene. *Nat. Commun.* **4,** 2811 (2013).
2. Zhang, T., Li, X. & Gao, H. Fracture of graphene: a review. *Int. J. Fract.* **196,** 1–31 (2015).
3. Ovid'ko, I. A. Mechancial properties of graphene. *Rev. Adv. Mater. Sci.* **34,** 1–11 (2013).
4. Cranford, S., Sen, D. & Buehler, M. J. Meso-origami: folding multilayer graphene sheets. *Appl. Phys. Lett.* **95,** 123121 (2009).
5. Ebbesen, T. W. & Hiura, H. Graphene in 3-dimensions: towards graphite origami. *Adv. Mater.* **7,** 582–586 (1995).
6. Blees, M. K. *et al.* Graphene kirigami. *Nature* **524,** 204–207 (2015).
7. Castle, T. *et al.* Making the cut: lattice kirigami rules. *Phys. Rev. Lett.* **113,** 245502 (2014).
8. Fasolino, A., Los, J. H. & Katsnelson, M. I. Intrinsic ripples in graphene. *Nat. Mater.* **6,** 858–861 (2007).
9. Hamm, E., Reis, P., LeBlanc, M., Roman, B. & Cerda, E. Tearing as a test for mechanical characterization of thin adhesive films. *Nat. Mater.* **7,** 386–390 (2008).
10. Kendall, K. Thin-film peeling-the elastic term. *J. Phys. D* **8,** 1449 (1975).
11. Sen, D., Novoselov, K. S., Reis, P. M. & Buehler, M. J. Tearing graphene sheets from adhesive substrates produces tapered nanoribbons. *Small* **6,** 1108–1116 (2010).
12. Chopra, N. G. *et al.* Fully collapsed carbon nanotubes. *Nature* **337,** 135–138 (1995).
13. Mikata, Y. New and improved analytical solutions for the self-folding problem of carbon nanotubes. *J. Nanomech. Micromech.* **3,** 04013004 (2013).
14. Meng, X., Li, M., Kang, Z., Zhang, X. & Xiao, J. Mechanics of self-folding of single-layer graphene. *J. Phys. D* **46,** 055308 (2013).
15. Cox, B. J., Baowan, D., Bacsa, W. & Hill, J. M. Relating elasticity and graphene folding conformation. *RSC Adv.* **5,** 57515–57520 (2015).
16. Chen, X., Yi, C. & Ke, C. Bending stiffness and interlayer shear modulus of few-layer graphene. *Appl. Phys. Lett.* **106,** 101907 (2015).
17. Chen, X., Zhang, L., Zhao, Y., Wang, X. & Ke, C. Graphene folding on flat substrates. *J. Appl. Phys.* **116,** 164301 (2014).
18. Lawn, B. R. *Fracture of Brittle Solids* (Cambridge Univ. Press, 1993).
19. Dietzel, D., Feldmann, M., Schwarz, U. D., Fuchs, H. & Schirmeisen, A. Scaling laws of structural lubricity. *Phys. Rev. Lett.* **111,** 235502 (2013).
20. Feng, X., Kwon, S., Park, J. Y. & Salmeron, M. Superlubric sliding of graphene nanoflakes on graphene. *ACS Nano* **7,** 1718–1724 (2013).
21. Liu, Z. *et al.* Observation of microscale superlubricity in graphite. *Phys. Rev. Lett.* **108,** 205503 (2012).
22. Yang, J. *et al.* Observation of high-speed microscale superlubricity in graphite. *Phys. Rev. Lett.* **110,** 255504 (2013).
23. Li, P., You, Z. & Cui, T. Adhesion energy of few layer graphene characterized by atomic force microscope. *Sens. Actuator. A* **217,** 56–61 (2014).
24. Vahdat, A. S. & Cetinkaya, C. Adhesion energy characterization of monolayer graphene by vibrational spectroscopy. *J. Appl. Phys.* **114,** 143502 (2013).
25. He, Y., Chen, W. F., Yu, W. B., Ouyang, G. & Yang, G. W. Anomalous interface adhesion of graphene membranes. *Sci. Rep.* **3,** 2660 (2013).
26. Bunch, J. S. & Dunn, M. L. Adhesion mechanics of graphene membranes. *Solid State Commun.* **152,** 1359–1364 (2012).
27. Huang, X., Yang, H., van Duin, A. C. T., Hsia, K. J. & Zhang, S. Chemomechanics control of tearing paths in graphene. *Phys. Rev. B* **85,** 195453 (2012).
28. Slotman, G. J. *et al.* Effect of structural relaxation on the electronic structure of graphene on hexagonal boron nitride. *Phys. Rev. Lett.* **115,** 186801 (2015).

METHODS

Graphene flakes were mechanically exfoliated from Kish bulk graphite samples by the scotch-tape method and deposited on Si wafers with 300 ± 5 nm oxide. The thinnest flakes were selected by optical microscopy (Zeiss Axio Imager) and mounted in a nanoindentation system (Fast Forward Devices). Constant strain rate indentation with simultaneous small amplitude lateral oscillation using a diamond Berkovich tip was performed on the graphene flakes and the residual impressions and self-assembled ribbons were measured by AFM (Asylum MFP 3D) using tapping mode silicon probes (Budget Sensors). The layer number of the graphene flakes and the stacking order of the ribbons were assessed via scanning Raman spectroscopy (WiTec Alpha 300R) to micrometre spatial resolutions.

Care was taken to avoid the presence of defects during the experiments. We have observed numerous occurrences of collisions between spontaneously growing ribbons and local defects including contaminants, other ribbons and flake steps and edges. In Extended Data Fig. 1 we show the effect of ribbon collision with small, observable contamination particles (composition unknown) through a series of AFM images that tracked ribbon shape and position as a function of time over 12 h. The images in Extended Data Fig. 1 also demonstrate that ribbons can do useful work to move contamination particles, as indicated by the dotted arrow. Growth speed is greatly reduced during these interaction periods, but then resumes a high speed once the particle is cleared. The force exerted by impeding objects often results in a deformation of the fold, as shown by the yellow arrow in the figure. This deformation disappears upon removal of the impediment and resumption of normal growth.

The relative intensities, peak shape and peak position from Raman spectra have been used to determine the thickness of graphene[28] and the stacking order between layers[30,31]. The ratio of the G to 2D band intensities and the full width at half maximum (FWHM) of the 2D band peak were used to determine the stacking order between the de-wetted graphene structures and the underlying flake[30,31].

An example of our Raman analysis for a mechanically exfoliated graphene flake with no self-assembled ribbons present is shown in Extended Data Fig. 2. An optical image of a mechanically exfoliated trilayer graphene sheet with a thicker four-layer strip is indicated in the optical micrograph in Extended Data Fig. 2a. A map of the G band intensity of this flake is shown in Extended Data Fig. 2b, which is a signature of the Raman characteristics of commensurately stacked graphene with an increase in the G band intensity within the thicker four-layer area. In contrast to this, the map of the 2D band, Extended Data Fig. 2c, shows a slight decrease in the 2D band intensity within the thicker four-layer area. This slight decrease is due to the stepwise broadening of the 2D band with increasing thickness, which results in an effective decrease in the 2D band intensity. This in turn results in an increase in the ratios of the G to 2D bands with increasing thickness, which were measured to be 1.6 and 2 within the three-layer and four-layer areas respectively. The broadening of the 2D band with increasing thickness can be seen by the map of the FWHM shown in Extended Data Fig. 2d and also by the plot of the averaged spectra within the three- and four-layer areas, shown in Extended Data Fig. 2e, f.

In Extended Data Fig. 3 we performed the same Raman analysis as described above on the three-ribbon growth sample shown in Fig. 1. Extended Data Fig. 3a shows an optical micrograph of the edge of the bilayer flake, where the three folded-over ribbon structures each form a four-layer stack. The map of the G band intensity, shown in Extended Data Fig. 3b is characteristic of the typical Raman signature of graphene with a larger G band intensity within the thicker folded-over sections of graphene. In contrast to the Raman signature of commensurately stacked graphene shown in Extended Data Fig. 2, the thicker folded-over graphene sheets result in a dramatic rise in the 2D band intensity, as shown in Extended Data Fig. 3d. In addition, the map of the FWHM of the 2D band shows no broadening within the thicker four-layer folded sections. The plots of the average spectra, shown in Extended Data Fig. 3e, f, highlight the similarity in the 2D band shape and G:2D ratios within the bilayer and four-layer areas, measured to be 1.44 and 1.47, respectively. The analysis indicates that the de-wetted graphene structures are incommensurate with the underlying flake and have not rotated into commensurability with the substrate.

For the ribbon growth kinetics, we present here a brief derivation of the rate activation analysis we used for the analysis of the data presented in Fig. 4, for single-bond breaking processes via the measurement of ribbon length and width versus time.

Fracture propagation can be considered as a stress-modified, thermally activated process of bond breaking with frequency[18]

$$K = \nu_0 \left[\exp\left(\frac{-\Delta F_+}{k_B T} \right) - \exp\left(\frac{-\Delta F_-}{k_B T} \right) \right] \tag{7}$$

where k_B is Boltzmann's constant, T is temperature and the natural lattice frequency is given

$$\nu_0 = \frac{k_B T}{h} \tag{8}$$

where $F_\pm$ are the molecular free energies of formation of a stress-activated adsorption complex from the reactants and products respectively. The stress dependence can be expressed as a Taylor expansion of the difference $G - R$ of the crack energy release rate G from crack resistance energy density R

$$\Delta F_\pm = \Delta F \mp \alpha(G - R) + \cdots \tag{9}$$

where ΔF is a quiescent adsorption-desorption activation energy at $G - R = 0$ and.

$$\alpha = \left(\frac{dF}{dG} \right) \tag{10}$$

is the activation length. To find the crack velocity, we write $\nu = K a_0$ where a_0 is the spacing between the bonds along the crack path. This gives

$$\nu = \nu_0 a_0 \left[\exp\left(\frac{-\Delta F}{k_B T} \right) \sinh\left(\frac{\alpha(G - R)}{k_B T} \right) \right] \tag{11}$$

The point $G = R$ is the quiescent point in ν–G space, giving a threshold for crack extension or retraction when the driving and resisting forces on the crack tip are balanced. From the static force analysis in the main text, we identify the individual bond rupture energy $\Delta F = \lambda a_0$. From equation (3), under quasi-static (slow) crack growth conditions for a 2D crack in a graphene sheet the energy release rate

$$G = \frac{\gamma_2 w \cos\theta}{2} + D \sin\theta \approx \frac{\gamma_2 w}{2} \tag{12}$$

and the resistance

$$R = \frac{\gamma_1 w \cos\theta}{2} + \beta w \approx \frac{\gamma_1 w}{2} + \beta w \tag{13}$$

where we assume possible resistance terms beyond the substrate peeling (such as the friction of ribbon head sliding and fold interlayer sliding) to scale with w over the range of observation with a proportionality constant β. Thus

$$\nu = \nu_0 a_0 \left[\exp\left(-\frac{\lambda a_0}{k_B T} \right) \sinh\left(\frac{\alpha(\Delta\gamma - \beta)w}{k_B T} \right) \right] \tag{14}$$

Quantitatively,

$$\nu_0 = \frac{k_B T}{h} \approx \frac{1/40 \text{ eV}}{4.14 \times 10^{-15} \text{ eV s}^{-1}} \approx 6 \times 10^{12} \text{ s}^{-1} \tag{15}$$

In the case of the bilayer graphene sample analysed in Fig. 4,

$$\nu_0 = \nu_0 a_0 \approx 6 \times 10^{12} \text{ s}^{-1} \times \frac{0.15 \text{ nm}}{2} \approx 4.2 \times 10^{11} \text{ nm s}^{-1} \tag{16}$$

where we have taken a mean bond length of 0.15 nm for single-layer graphene and doubled the number of bonds encountered by the crack in a bilayer sheet.

The direct measurement of the ribbon crack tip velocity versus time is hampered by a poor signal to noise ratio when taking a numerical derivative of our limited-precision AFM fold-position measurements. If we assume a constant taper angle over the range of ribbon growth measured, we can perform a numerical fitting procedure of the data to the path length versus the time of the integral of a logarithmic version of equation (14), which is a good approximation when the argument to the sinh function is greater than two, as we expect from the magnitude of the velocity we observe. For a fitted form to fold position l (giving approximately the path length for the small taper angle present) we use

$$l = a \log[b(t - t_0)] + l_0 \tag{17}$$

where (t_0, l_0) represent the point at which our quasi-static model begins to properly apply to the ribbon growth and a and b are fitting constants. We do not necessarily expect $(t_0, l_0) = (0 \text{ s}, 0 \text{ nm})$ due to possible unaccounted for high-speed growth physics, however we do assume that all of the measured growth data (on the order of minutes or more) has already reached the quasi-static regime. Extended Data Fig. 4 shows the results of fitting for the ribbon fold position and velocity to the measured data for the system presented in Fig. 4, as well as a similar procedure applied to the shrinking ribbon width w.

From the fit of velocity versus width in Fig. 4, we extract $\lambda a_0 = 3.0\,\mathrm{eV}$ and $\alpha(\Delta\gamma - \beta) \approx 0.0021\,\mathrm{eV}\,\mathrm{nm}^{-1}$. Assuming a mean bond spacing of around 0.1 nm gives a bond-rupture energy density of $\lambda \approx 30\,\mathrm{eV}\,\mathrm{nm}^{-1}$, which is compatible with simulations of the graphene tearing resistance. The drag term β embodies the resistance due to finite sliding friction[19,32] and other possible dissipative processes. Ignoring this term and assuming that the activation length α to be the bond spacing 0.1 nm, we find that $\Delta\gamma = 0.021\,\mathrm{eV}\,\mathrm{nm}^{-2}$.

29. Ferrari, A. C. *et al.* Raman spectrum of graphene and graphene layers. *Phys. Rev. Lett.* **97,** 187401 (2006).
30. Ni, Z, Wang, Y., Yu, T., You, Y. & Shen, Z. Reduction of Fermi velocity in folded graphene observed by resonance Raman spectroscopy. *Phys. Rev. B* **77,** 235403 (2008).
31. Hao, Y. *et al.* Probing layer number and stacking order of few-layer graphene by Raman spectroscopy. *Small* **6,** 195–200 (2010).
32. van den Ende, J. A., De Wijn, A. S. & Fasolino, A. The effect of temperature and velocity on superlubricity. *J. Phys. Condens. Matter* **24,** 445009 (2012).
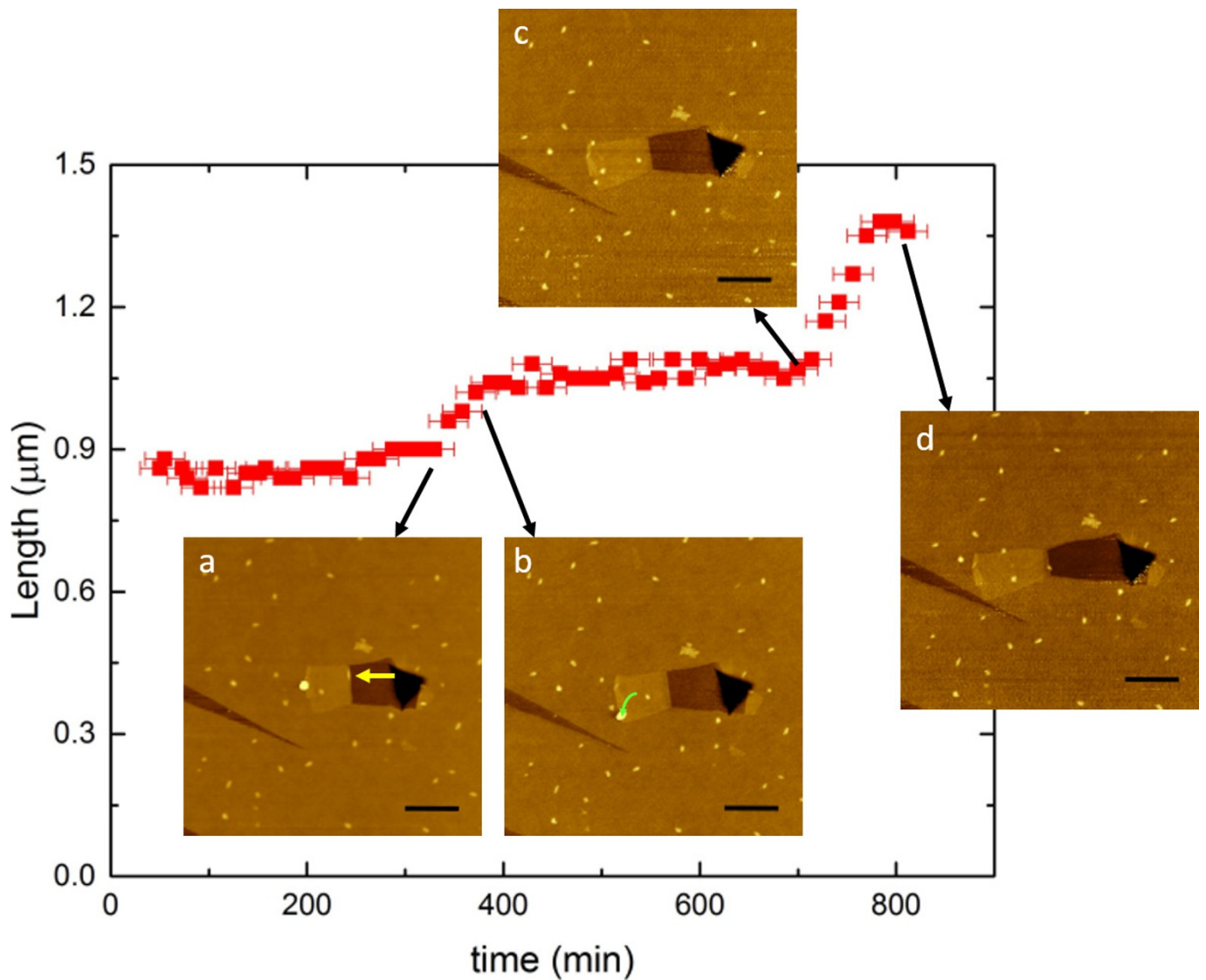
Extended Data Figure 1 | Ribbon growth and collision with visible contaminants. The growth pattern recorded by AFM imaging shows ribbon pinning and release as contamination defects are pushed aside (insets **a** and **b**), followed by rapid growth until next contaminant reached at point **c**. Final ribbon pinning occurs by encounter with sliver fracture in the flake that exposes the underlying substrate **d**. In **a**, a bulge in the fold (yellow arrow) has been disappeared by **b** as the defect has moved to a lower position along the ribbon head indicated by the green arrow. Ribbon growth direction is to the left. Horizontal error bars indicate uncertainty in exact time of AFM image acquisition used to extract ribbon length values, whereas vertical error bars are omitted as the uncertainty range is too small to see at this scale.
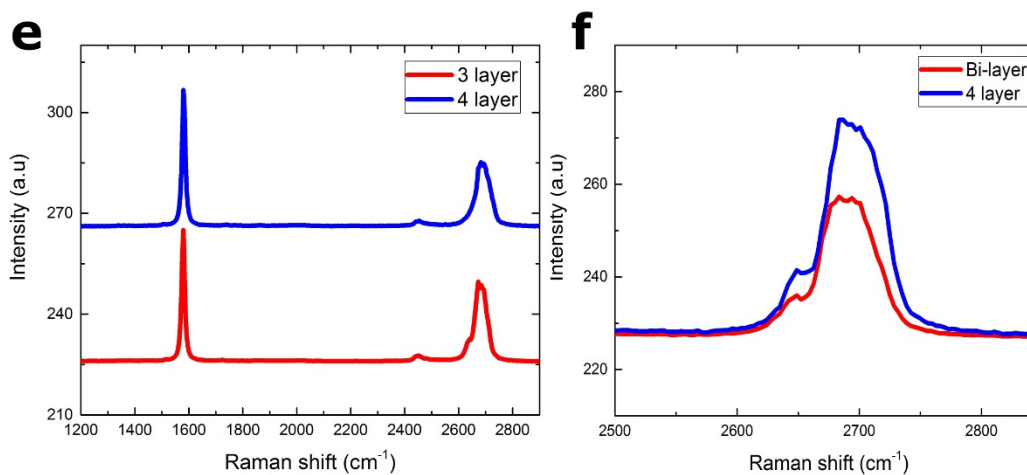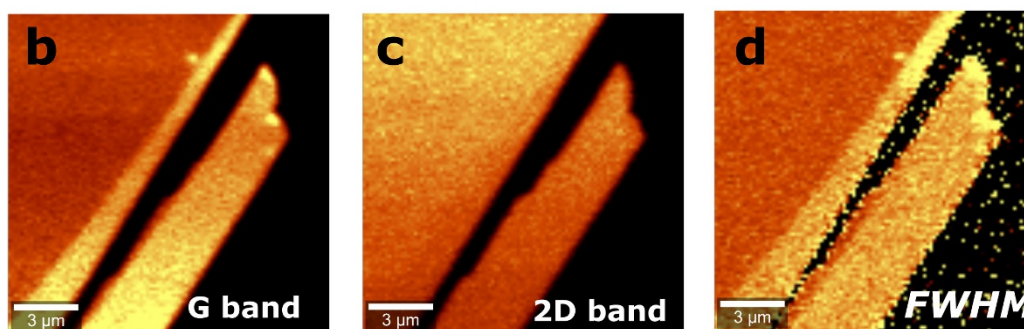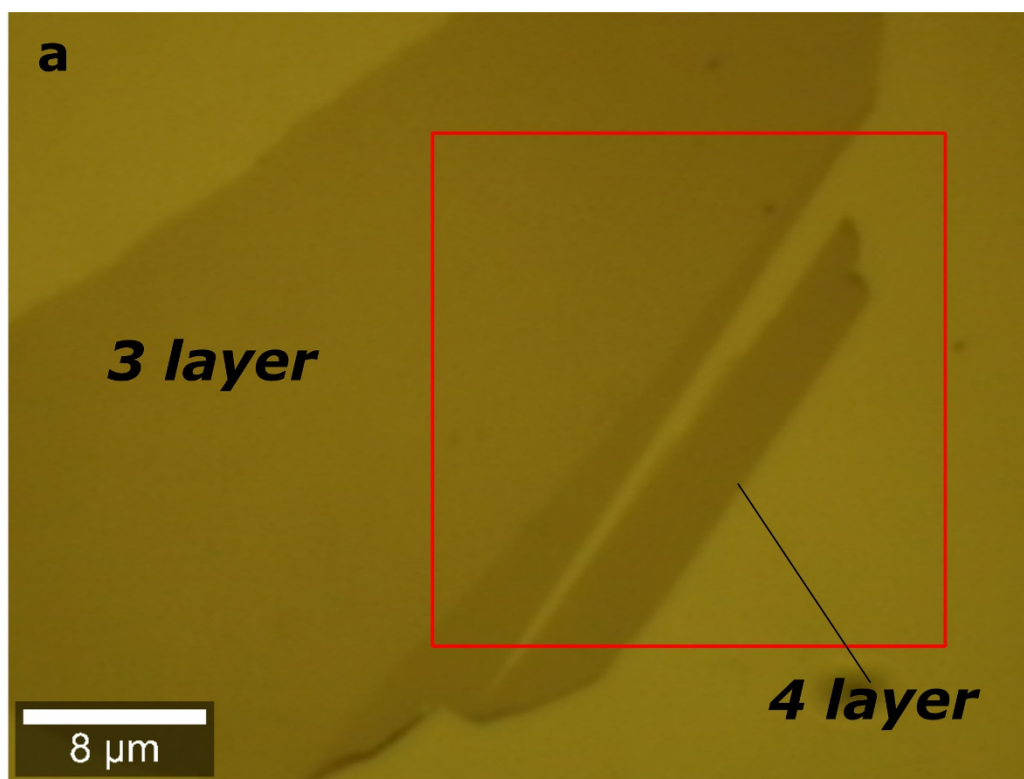
Extended Data Figure 2 | Scanning Raman analysis of commensurate stacked layers in a mechanically exfoliated graphene flake with no self-assembled structures present. a, Optical micrograph of a mechanically exfoliated graphene sheet. The red box indicates the area that was analysed, comprising three- and four-layer-thick graphene sheets. **b–d**, Maps of the G band intensity (**b**), 2D band intensity (**c**) and the FWHM of the 2D band (**d**). **e**, Plot of the average Raman spectra within the three- and four-layer areas. **f**, Comparative plot of the 2D bands within the three- and four-layer areas.
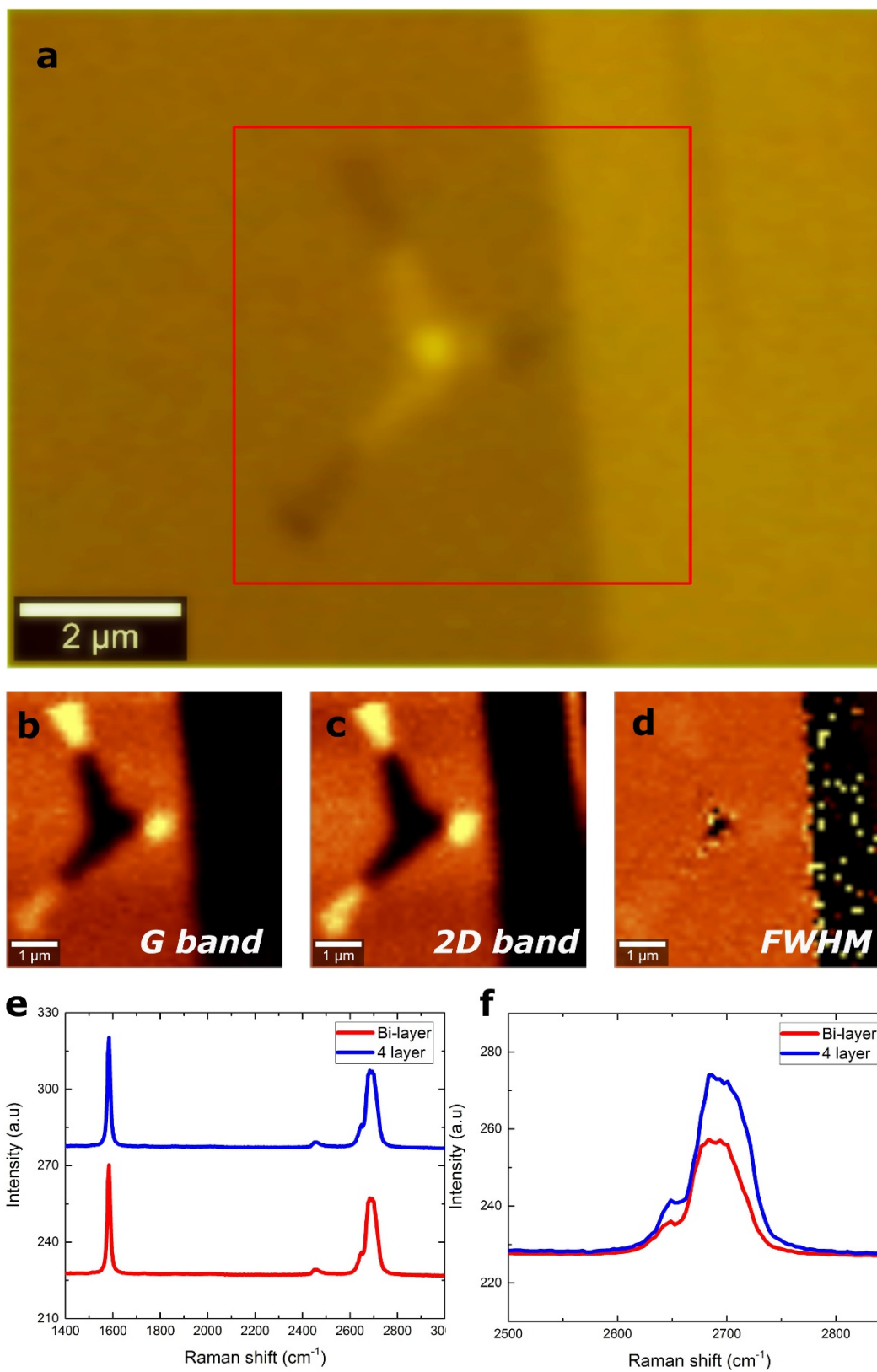
Extended Data Figure 3 | Scanning Raman analysis of the self-assembled bilayer graphene ribbons shown in Fig. 1l. a, Optical micrograph of the mechanically exfoliated bilayer graphene sheet. The red box indicates a single indentation from which the three folded ribbons grew. **b–d**, Maps of the G band intensity (**b**), 2D band intensity (**c**) and the FWHM of the 2D band (**d**). **e**, Plot of the average Raman spectra within the folded ribbons (four-layer) and the bilayer sheet. **f**, Comparative plot of the 2D bands within the folded ribbons four-layer) and the bilayer sheet.
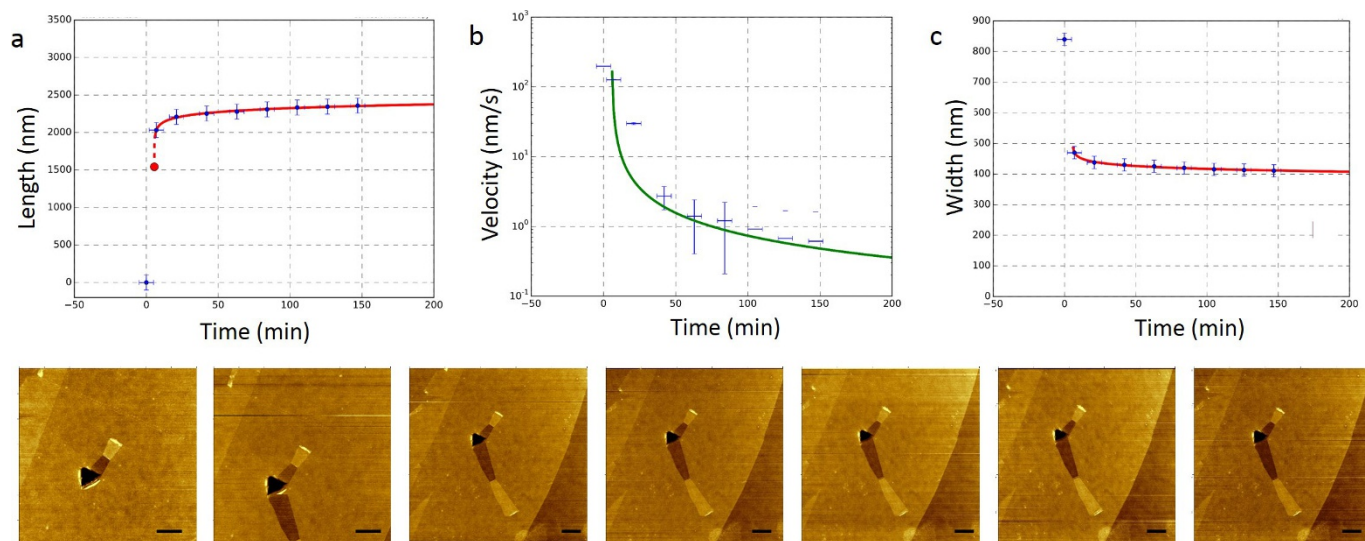
Extended Data Figure 4 | Fits to the ribbon head position. a–c, Ribbon length (**a**), velocity (**b**) and width (**c**) versus time for the self-assembling ribbon system presented in Fig. 4, as extracted from the sequence of AFM images shown below. See Methods for an explanation of the fitting functions. Scale bars, 1 μm.